Ambient Vibration Modal Analysis of Natural Rock Towers and Fins

Riley Finnegan[*1], Jeffrey R. Moore[1], Paul R. Geimer[1,2], Alex Dzubay[1], Erin K. Bessette-Kirton[1], Jackson Bodtker[1,3], and Kathryn Vollinger[4]

Abstract

The dynamic properties of freestanding rock towers are important inputs for seismic stability and vibration hazard assessments, however data describing the natural frequencies, mode shapes, and damping ratios of these landforms remain rare. We measured the ambient vibration of 14 sandstone and conglomerate rock towers and fins in Utah, United States, using broadband seismometers and nodal geophones. Fundamental frequencies vary between 0.8 and 15 Hz—inversely with tower height—and generally exhibit subhorizontal modal vectors oriented parallel to the minimum tower width. Modal damping ratios are low across all features, between 0.6% and 2.2%. We reproduced measured modal attributes in 3D numerical eigenfrequency models for 10 of the 14 landforms, showing that the fundamental mode of these features is full-height bending akin to a cantilever. Fin-like landforms commonly have a torsional second mode whereas tower-like features have a second full-height bending mode subperpendicular to the fundamental. In line with beam theory predictions, our data confirm that fundamental frequencies scale with the ratio of a tower's width to its squared height. Compiled data from 18 other sites support our results, and taken together, provide guidance for estimating the modal properties of rock towers required for vibration risk assessment and paleoseismic shaking intensity analysis in different settings.

Cite this article as Finnegan, R., J. R. Moore, P. R. Geimer, A. Dzubay, E. K. Bessette-Kirton, J. Bodtker, and K. Vollinger (2022). Ambient Vibration Modal Analysis of Natural Rock Towers and Fins, *Seismol. Res. Lett.* **XX**, 1–10, doi: 10.1785/0220210325.

Supplemental Material

Introduction

Rock towers, fins, and slabs are commonly associated with slope instability hazards in places such as coastal bluffs, caprock rims, cliffs, and erosional landscapes, and in many instances represent culturally valued geologic landforms (e.g., Carmean, 2002; Lévy *et al.*, 2010; Bottelin *et al.*, 2013; Branch and Cordalis, 2017; Moore *et al.*, 2019; Colombero *et al.*, 2021). These features may thus be assessed for seismic stability or risk of vibration damage (e.g., Dowding *et al.*, 1983; Moore *et al.*, 2016; Finnegan *et al.*, 2021), and in addition are increasingly being probed as proxies of regional paleoseismic shaking intensity (e.g., Brune, 1996; Baker *et al.*, 2013; Finzi *et al.*, 2020; Rood *et al.*, 2020; McPhillips and Scharer, 2021). In each case, accurate vibration assessment requires knowledge of the landform's dynamic properties, including natural frequencies, modal polarization attributes, and damping ratios, which control whether the structure will resonate in response to various energy inputs (Chopra, 2012). Understanding the resonance susceptibility of a feature is thus a critical first step in evaluating the potential for vibration damage and seismic stability. However, experimental datasets describing the dynamic properties of rock landforms are rare, in part because of challenging and limited site access (compare with Michel *et al.*, 2008).

The dynamic properties of freestanding rock landforms can be extracted from ambient vibration data (e.g., Kleinbrod *et al.*, 2019; Geimer *et al.*, 2020; Bottelin *et al.*, 2021; Colombero *et al.*, 2021; Häusler, Geimer, *et al.*, 2021). In Utah, for example, Moore *et al.* (2019) analyzed data from a 120-m-high sandstone tower, describing the first two natural modes. Similar studies from the Vercors Massif in France reported natural frequencies and mode shapes of several limestone columns (Lévy *et al.*, 2010; Bottelin *et al.*, 2013, 2017), and a similarly tall, slender carbonate pillar was recently evaluated in Israel (Finzi *et al.*, 2020). Engineering consulting studies have additionally reported natural frequencies and damping ratios from rock pinnacles in granite and rhyolite from southeastern Arizona (King, 2001, 2003), along with a single tower measured in the lime-rich sedimentary rocks of Bryce Canyon National Park, Utah (Dowding *et al.*, 1983). Several studies

1. Department of Geology and Geophysics, University of Utah, Salt Lake City, Utah, U.S.A., https://orcid.org/0000-0003-3234-6439 (RF); https://orcid.org/0000-0001-5831-2048 (JRM); https://orcid.org/0000-0003-2627-5507 (PRG); https://orcid.org/0000-0001-6656-312X (AD); https://orcid.org/0000-0002-2797-0694 (EKB-K); https://orcid.org/0000-0002-1576-0550 (JB); 2. Los Alamos National Laboratory, Los Alamos, New Mexico, U.S.A.; 3. Department of Earth Sciences, University of Calgary, Calgary, Alberta, Canada; 4. Leavenworth, Washington, U.S.A.

*Corresponding author: riley.finnegan@utah.edu

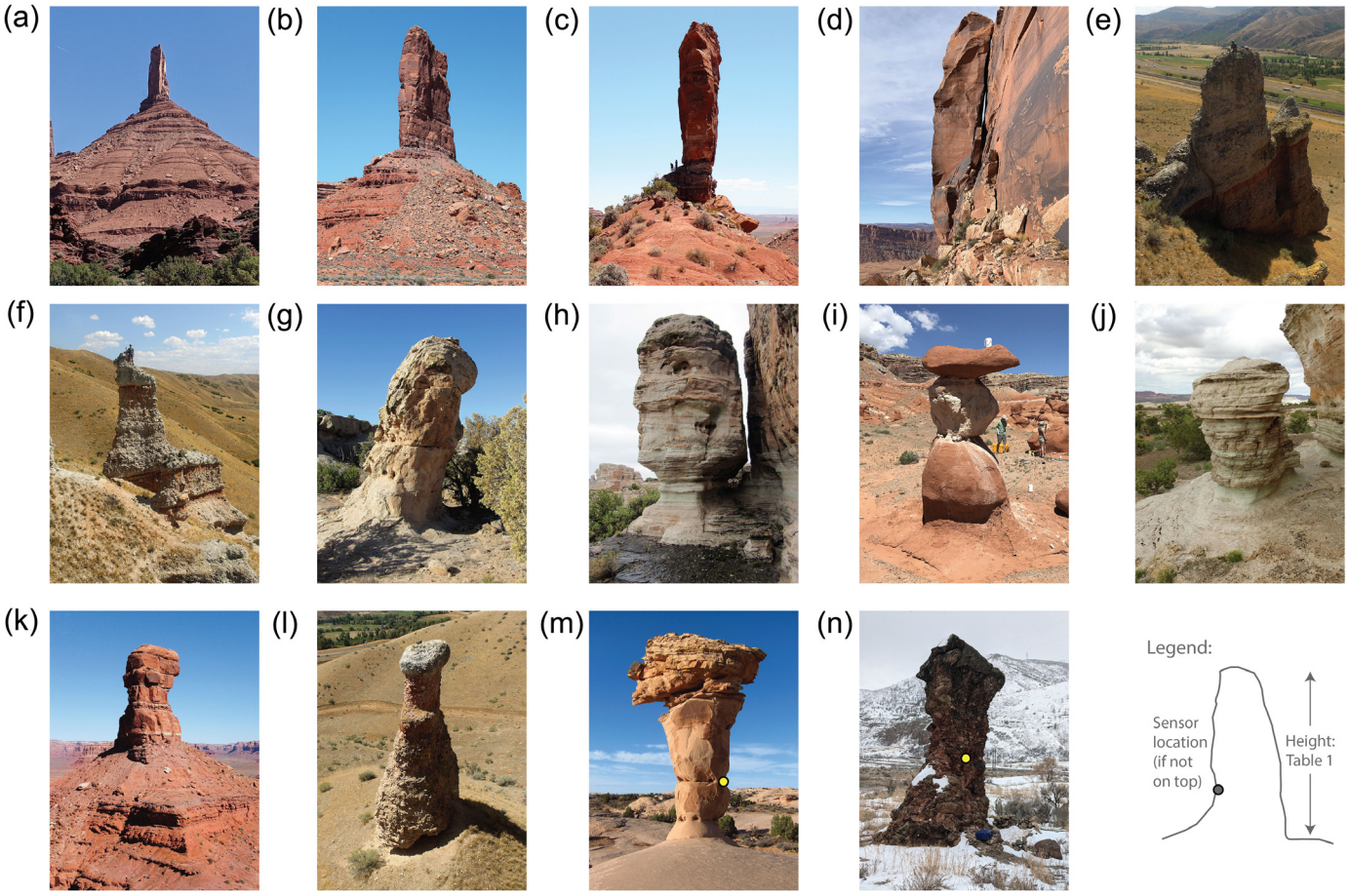

Figure 1. Photographs of all study sites: (a) Castleton Tower, (b) Eagle Plume Tower, (c) Tides of Mind, (d) Kane Springs Ledge, (e) Unnamed Witch, (f) Skinny Witch, (g) Juniper Tower, (h) Courthouse Tower 1, (i) Bike Seat, (j) Courthouse Tower 3, (k) Petard Tower, (l) Wicked Witch, (m) Secret Spire, (n) Red Narrows Tower. Data from (a–j) were successfully reproduced in 3D eigenfrequency models whereas (k–n) were successfully measured but could not be reproduced in eigenfrequency models. Sensors were placed on top of each landform except for (m) and (n) where the sensor location is noted. Sites (a–j) and (k–n) are ordered by descending height, given in Table 1. The color version of this figure is available only in the electronic edition.

use similar methods to evaluate the dynamic properties of stalagmite cave formations (e.g., Gribovszki *et al.*, 2018; Martin *et al.*, 2020). Damping ratios are less frequently described: for slender rock landforms with few fractures, such as rock arches and towers, modal damping has been shown to be low (~1%–3% of critical damping; Moore *et al.*, 2019; Geimer *et al.*, 2020; Häusler, Geimer, *et al.*, 2021), but can reach values of 8%–10% for fractured rock slope instabilities (Häusler, Michel, *et al.*, 2021).

Here, we analyze in situ ambient vibration data from 14 freestanding rock towers and fins in Utah (Fig. 1; Table 1), composed of sandstone and conglomerate, and compare our new data with studies of similar features in other lithologies. The combined dataset, containing 32 sites, describes the range of natural frequencies typical for these landforms, demonstrates relationships between fundamental frequencies and scale, and adds important new field measurements of damping. We hypothesize that the fundamental mode of rock towers and fins is full-height Euler–Bernoulli bending akin to a cantilever beam, and that analytical expressions can be useful for first-order assessment, and predict that slender towers differ from fins and slabs at higher modes (i.e., second-order bending and torsional modes). We further hypothesize that these rock landforms exhibit low-damping ratios that may generate large spectral amplifications. These modal properties are crucial inputs for dynamic stability assessments in support of conservation and hazard evaluations, as well as paleoseismic shaking intensity estimates.

Study Sites

We measured ambient vibrations of 14 rock towers and fins in Utah, United States (Fig. 1; Table 1). These landforms are located on the traditional lands of the Eastern Shoshone, Hopi, Navajo, Southern Paiute, Ute, and Zuni peoples, and many have cultural and religious significance to these groups (e.g., Branch and Cordalis, 2017). Sites were classified as tower-like (slender in both horizontal dimensions) or fin-like (asymmetrically long in one direction); we define the minor cross-

TABLE 1
Sites Assessed in This Study

Site Name	Class	Instrument	Latitude, Longitude (dd)	Geologic Unit	Height (m)	Width (m)	w/h^2 (m^{-1})	Azimuth (degrees)	Start Time (yyyy/mm/dd) Time (UTC) (hh:mm:ss)	Duration (min)	f_0 (Hz)	RDT Damping (%)	E (GPa)
Castleton Tower	Tower	TC20	38.6510, −109.3679	Wingate Sandstone	120	38	0.0026	–	2018/03/12 20:30:00	160	0.81	0.8	7.0
Eagle Plume Tower	Fin	TC20	37.3145, −109.8540	Cedar Mesa Sandstone	85	20	0.0028	110	2020/10/29 20:07:00	120	0.90	0.6	7.0
Tides of Mind	Fin	TC20	37.3246, −109.8640	Cedar Mesa Sandstone	25	4	0.0064	115	2020/10/30 18:25:00	110	0.75	0.9	0.7
Kane Springs Ledge	Tower	TC20	38.4817, −109.5950	Wingate Sandstone	20	6	0.0150	140	2021/01/16 20:30:00	1350	1.79	1.0	1.4
Unnamed Witch	Fin	TC20	40.9953, −111.4564	Henefer Formation conglomerate	11	3.8	0.0314	215	2018/09/03 19:00:00	30	4.58	2.2	2.0
Skinny Witch	Fin	TC20	40.9953, −111.4561	Henefer Formation conglomerate	11	2.5	0.0207	350	2018/09/03 20:15:00	30	3.59	1.6	1.5
Courthouse Tower 1	Tower	Zland	38.7022, −109.7381	Curtis Formation	5.5	1.5	0.0496	80	2018/10/11 00:00:00	960	5.83	1.1	0.9
Juniper Tower	Tower	TC20	38.6889, −109.9629	Navajo Sandstone	5.5	2	0.0661	10	2021/04/12 14:35:00	70	7.71	1.4	2.2
Bike Seat	Tower	Zland	38.0782, −110.6282	Entrada Sandstone	3.3	1	0.0918	–	2019/06/05 17:00:00	60	10.51	1.3	1.0
Courthouse Tower 3	Fin	Zland	38.7029, −109.7371	Curtis Formation	2.6	0.85	0.1257	200	2018/10/11 16:45:00	25	14.58	1.5	0.8
Petard Tower	Tower	TC20	37.2761, −109.8112	Cedar Mesa Sandstone	45	21	0.0104	–	2020/10/31 18:35:00	120	1.99	0.9	–
Wicked Witch	Tower	TC20	40.9956, −111.4566	Henefer Formation conglomerate	11.5	3	0.0227	–	2018/09/03 16:14:00	35	5.50	1.4	–
Secret Spire	Tower	TC20	38.6833, −109.9629	Navajo Sandstone	6.5	1.2	0.0284	–	2021/04/13 00:45:00	30	2.50	2.1	–
Red Narrows	Tower	TC20	39.9991, −111.4075	North Horn Formation conglomerate	5	1	0.0400	335	2021/02/20 16:06:00	34	7.90	2.1	–

Azimuth indicates overall orientation of the landform (where available) defined as the heading of the major horizontal axis and reported in degrees from magnetic north. Features with more cylindrical cross section have no azimuth listed. Young's modulus (E) given for features successfully reproduced with numerical eigenfrequency models. RDT, random decrement technique.

sectional axis of each landform as the minimum horizontal width, and the major axis as the maximum width. About 10 features are composed of sandstone and four are conglomerate. We selected sites that had both simple, prismatic geometry as well as more irregular shapes, with heights varying between 2.6 and 120 m (Table 1). At all but two sites (Red Narrows and Secret Spire), we were able to place a seismometer directly on top of the landform (Fig. 1). In most cases, this required the assistance of skilled climbers to haul, deploy, and retrieve the instruments, waiting quietly on the summit while the recording was taking place.

We sourced additional data on the natural frequencies and geometry of rock towers, pillars, and pinnacles (terms used interchangeably in literature) from previously published scientific studies and consulting reports (Table S1, available in the supplemental material to this article). These included seven smaller granitic pinnacles along the General Hitchcock Highway near Tucson, Arizona (King, 2003), four rhyolite pinnacles in Chiricahua National Monument, Arizona (King, 2001), a carbonate hoodoo in Bryce Canyon National Park, Utah (Dowding *et al.*, 1983), and a carbonate pillar in the Negev Desert of Israel (Finzi *et al.*, 2020). We also included related datasets for three pillar-like slope instabilities in limestone of the Vercors Massif in France (Lévy *et al.*, 2010; Bottelin *et al.*, 2013, 2017), as well as two measurements of cave stalagmites (Gribovszki *et al.*, 2018; Martin *et al.*, 2020). Although the fundamental frequency and height of each feature was reported in all cases, geometry was not uniformly described. In particular, King (2003) did not report width measurements for pinnacles of the Hitchcock dataset; therefore we enlisted help from a local assistant team to measure the width of each feature using a tape measure.

Methods

To determine the modal properties (i.e., natural frequencies, mode shapes, and damping ratios) of each landform, we used a combination of experimental and numerical modal analysis techniques (Moore *et al.*, 2018). Because site access was often limited, we generated ambient vibration data from sparse seismometer arrays (Geimer *et al.*, 2020), where at minimum one sensor was placed on the feature being assessed, ideally on top of the tower. We used three-component Nanometrics Trillium Compact 20 s seismometers (TC20; Table 1) paired with 24-bit Centaur data loggers for most measurements, with Fairfield ZLand 5 Hz three-component nodal geophones (ZLand) deployed at sites with limited surface access (Ward and Lin, 2017; Wu *et al.*, 2017). Sensors were placed on the rock surface, leveled and aligned to magnetic north, covered with a bucket (where space allowed) and left to record continuous ambient vibration data for durations between 25 min and 22.5 hr (Table 1).

We processed ambient vibration data for spectral content and polarization attributes. We first removed the mean and trend from each trace, removed the instrument response, and then band-passed data typically between 0.1 and 40 Hz. We then computed the power spectral density (PSD) using fast Fourier transforms (FFT) over hour-long data blocks when that length was available, and the maximum ambient vibration record length elsewhere (Koper and Burlacu, 2015). Because of varying sampling rates, the number of points per FFT window ranged from 2048 to 8192. We then averaged the spectra from 80% overlapped windows. For polarization analysis to describe mode shapes, we computed polarization attributes at selected frequencies (Koper and Hawley, 2010; Incorporated Research Institutions for Seismology Data Management Center [IRIS-DMC], 2015) using the same window parameters as the PSDs. We determined the degree of polarization (dimensionless ranging from 0 to 1), the orientation of motion in the horizontal plane (azimuth from north), and the incidence angle of particle motion (degrees from vertical; see Figs. S1–S14).

Damping results from thermal and viscoelastic energy dissipation as well as geometric effects and material contrasts (Çelebi, 2000; Ambrosini, 2006; Häusler, Michel, *et al.*, 2021), and can be measured from ambient vibration data (e.g., Häusler, Geimer, *et al.*, 2021). We used the random decrement technique (Cole, 1973) to calculate damping for each feature. Random decrement can be used to identify the damping ratio of a system using its free response, based on the assumption that the vibrational response of a system at any moment is the sum of random noise and its impulse response. Stacking many time windows with identical initial conditions and applying a band-pass filter around the natural frequency enhances the contribution of the impulse response relative to the noise. An exponentially decaying sinusoid is then fitted to the resulting response function to estimate the damping ratio (Mikael *et al.*, 2013). For each tower, we rotated horizontal data to the polarization azimuth of the fundamental mode and fit the sinusoid to 15-cycle windows stacked over a 10 min time period, filtered around the fundamental frequency. We computed damping in this way for all 10 min intervals available for each tower and reported the average damping ratio along with the population standard deviation.

We performed numerical modal analysis using commercial finite-element software (COMSOL Multiphysics: see Data and Resources). These models represent a test of whether the measured spectral and polarization attributes can be reproduced by simple, isotropic materials given a realistic geometry. To create 3D surface models of each tower, we generated georeferenced ground- and drone-based images and aligned photosets using commercial structure-from-motion photogrammetry software (Bentley Context Capture: see Data and Resources). We refined models in Meshmixer (see Data and Resources): for example, filling holes from incomplete photo coverage, smoothing irregular facets, and transforming the surface into a solid 3D object. We relied on field assessments to crop the final model, removing areas of adjacent ground not participating in vibrational modes. We verified model scaling for each

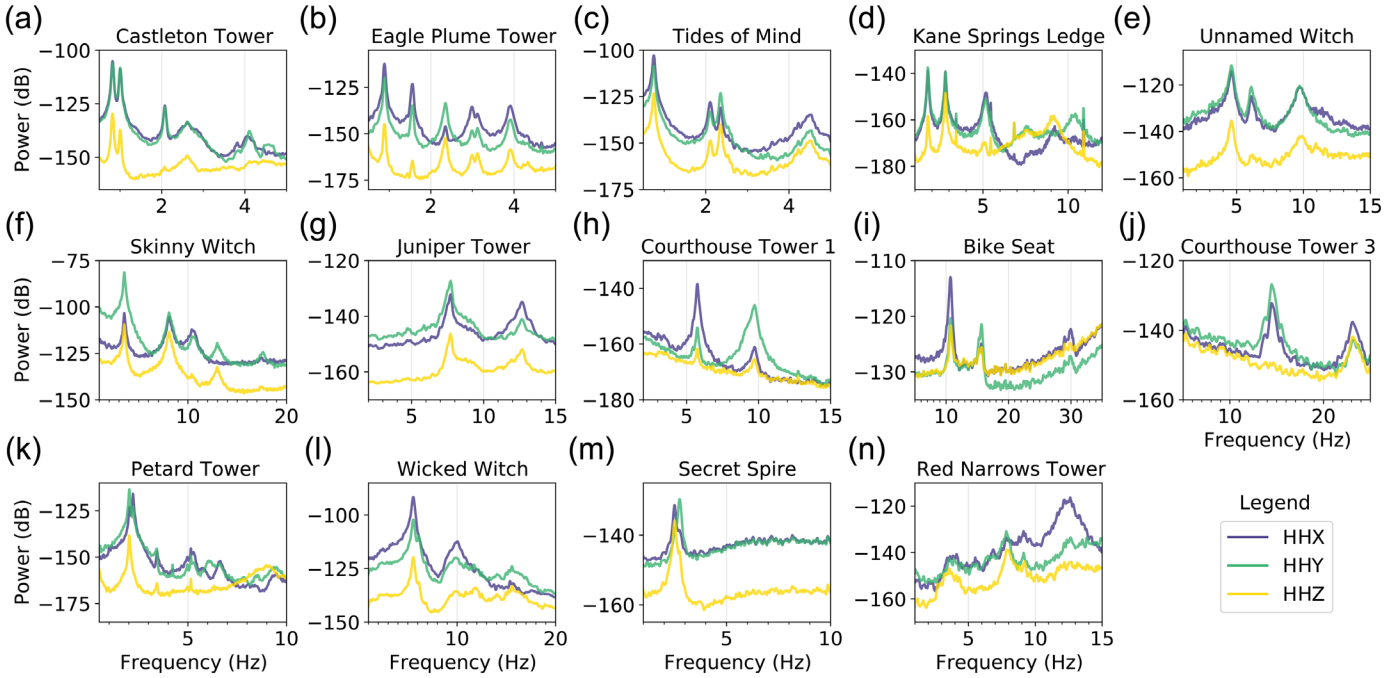

Figure 2. Velocity power spectral density estimates for all measured landforms, relative to magnetic north and with decibel powers relative to 1 m^2s^{-2} Hz^{-1}. Features (a–n) are ordered following the photographs in Figure 1. The color version of this figure is available only in the electronic edition.

feature from field measurements using tape measures for smaller landforms and a TruPulse 360 laser rangefinder for larger landforms. For towers and fins situated on sloping hillsides, we measured both the uphill (minimum) and downhill (maximum) height, as well as the horizontal width of each face.

Within COMSOL, we imported the geometrical models of each feature, then assigned material properties and selected regions of fixed boundary conditions, and solved the 3D eigenfrequency solution (i.e., in the frequency domain, with no input motion). We used an iterative procedure allowing Young's modulus (E) to vary until the best match was found to the first ~3 natural frequencies, keeping density (which is in general well known and varies only marginally) constant at 2000 kg/m^3 across all sites (Moore *et al.*, 2018). We then assessed the match between computed modal vectors at the location of the seismometer and field polarization data (azimuth and incidence; Geimer *et al.*, 2020). Outputs included visualizations of the modal deformation fields (for modes matching field data) as well as prediction of modes that may have been missed in field measurements, for example, if a sensor was located at a node point.

Simple analytical models are additionally useful for predicting the modal properties of rock landforms. For towers and fin-like features, the analytical approximation of a cantilever has been demonstrated to adequately reproduce measured natural frequencies (e.g., Dowding *et al.*, 1983; Bottelin *et al.*, 2013; Moore *et al.*, 2019; Finzi *et al.*, 2020; Martin *et al.*, 2020). The fundamental frequency (f_0) of an Euler–Bernoulli cantilever is simply a function of geometrical and material properties defined as (Chopra, 2012)

$$f_0 = \frac{1.875^2}{2\pi}\sqrt{\frac{EI}{\rho A h^4}}, \tag{1}$$

in which E is the Young's modulus, ρ is the density, h is the length (here tower height), A is the cross-sectional area, and I is the area moment of inertia. Assuming a rectangular cross section, $I = bw^3/12$, in which w is the thickness against which bending occurs (and b is the orthogonal thickness). Equation (1) can then be rewritten as

$$f_0 = \frac{1.875^2}{2\pi\sqrt{12}}\sqrt{\frac{E}{\rho}}\frac{w}{h^2}. \tag{2}$$

This relationship predicts that for features with similar material properties (e.g., similar rock types), fundamental frequencies scale with a geometrical ratio of w/h^2, and that variations in Young's modulus (i.e., soft vs. stiff rocks) are expressed as a change in slope of the scaling relationship. Although most features in our study are best represented by a rectangular cross section, assuming a circular cross section simply changes the $\sqrt{12}$ factor to 4 in equation (2).

Results

PSD estimates for each tower and fin measured in this study are shown in Figure 2, from which we identified fundamental and higher order natural frequencies. The tallest tower (Castleton Tower; 120 m high) has a fundamental frequency

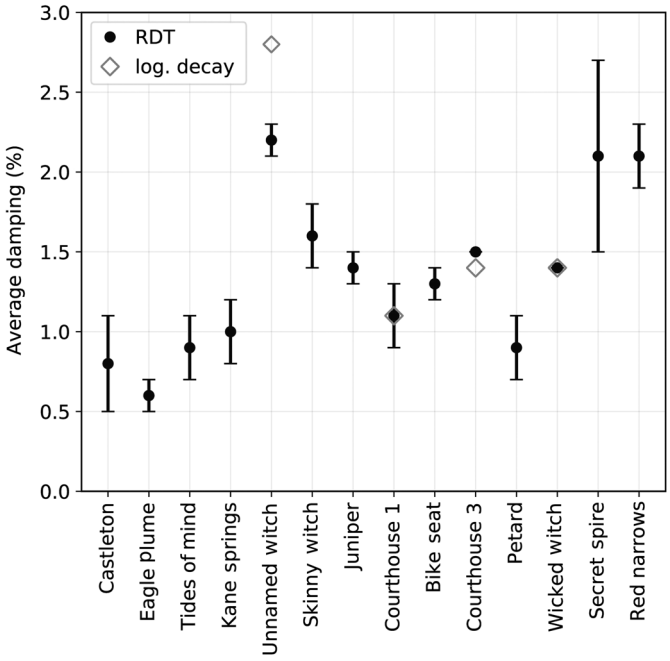

Figure 3. Damping measurements for all towers (see Fig. 1 and Table 1 for images and geometries). Error bars are determined as the population standard deviation for each individual random decrement technique (RDT) measurement. Damping measurements from logarithmic decay (log. decay) of manual impulses method included when available.

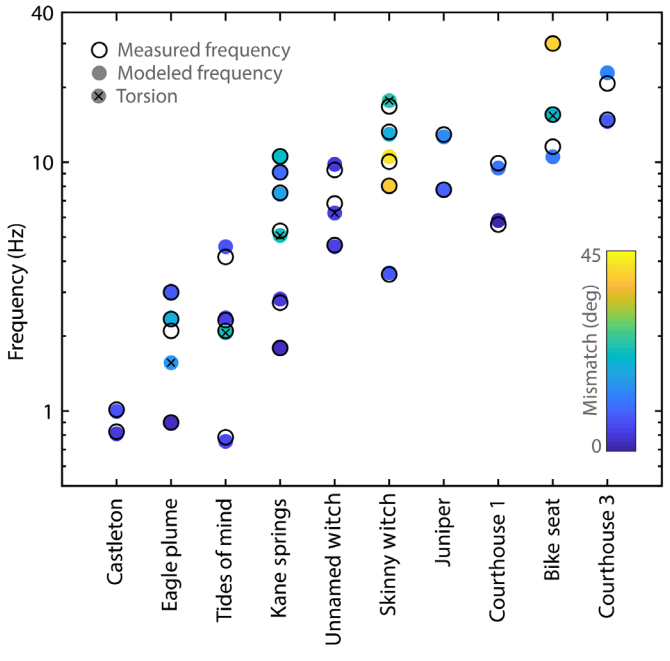

Figure 4. Measured and modeled natural frequencies for the 10 features successfully reproduced in this study (see also Table S2). Open circles show measured values, filled circles are modeled; color shading reflects the mismatch angle (in degrees) between the measured and modeled 3D modal vectors. Modeled torsional modes are indicated by an x. The color version of this figure is available only in the electronic edition.

of 0.8 Hz (Moore *et al.*, 2019), whereas the smallest tower measured (Courthouse Tower 3; 2.6 m high) has a fundamental frequency of 14.6 Hz (Table 1). We find a number of higher order modes in the recorded spectra, often more prominent for features with fin-like geometry. Polarization information (Figs. S1–S14) for the identified natural frequencies shows that modal vectors are generally aligned with the geometry of the landform, for example, the fundamental mode is oriented parallel to the minor axis for both fins and towers (compare landform orientation in Table 1 to modal azimuths in Table S2). We additionally measured damping ratios for each site, finding that these landforms have overall low damping, with ratios between 0.6% and 2.2% of critical (Fig. 3). For several smaller towers, we verified damping from the logarithmic decay of manual impulses (Silva, 1999), which produced similar values as the random decrement technique (Fig. 3).

As single-station field data provide mode shape information at only one point, we used numerical modal analysis to predict and fully visualize modal deformations. We achieved a close match between numerical model results and field data for 10 out of the 14 features studied (Fig. 1a–j). These models reproduced the natural frequencies, modal azimuth, and incidence angles within reasonable similarity, indicating that homogeneous models are sufficient to replicate the dynamic behavior of these landforms (Fig. 4; Table S2). Modeled eigenfrequencies matched measured values for the 10 towers generally within 10% (mean overall frequency mismatch of 4%), and modeled 3D modal vectors differed from measured orientations by a mean value of 14° (Fig. 4). When calibrated to match field data, the models additionally produced an estimated global rock mass Young's modulus for the feature (Table 1; Moore *et al.*, 2018). Of the four features not successfully modeled (Fig. 1k–n), one had an incomplete photogrammetric geometry (therefore no model could be run), one had unknown sensor alignment (field data could not be compared to model results), and two simply failed to match field data indicating the assumption of uniform composition failed in those cases.

For the 10 successfully modeled features, we were able to achieve a good match to the first two eigenmodes in all cases, and in the best case we matched the first six modes (Fig. 4). The resulting Young's modulus values for most features were ~1–2 GPa, whereas the two largest landforms had notably greater modulus of 7 GPa (Table 1). Example model results for Eagle Plume Tower (fin-type geometry) are shown in Figure 5 (see also supplemental animations S1–S4). For this feature, the fundamental mode is full-height bending against the minor axis, the second mode is torsion, the third mode is full-height bending against the major axis, and the fourth mode is second-order bending against the minor width. Importantly, these models

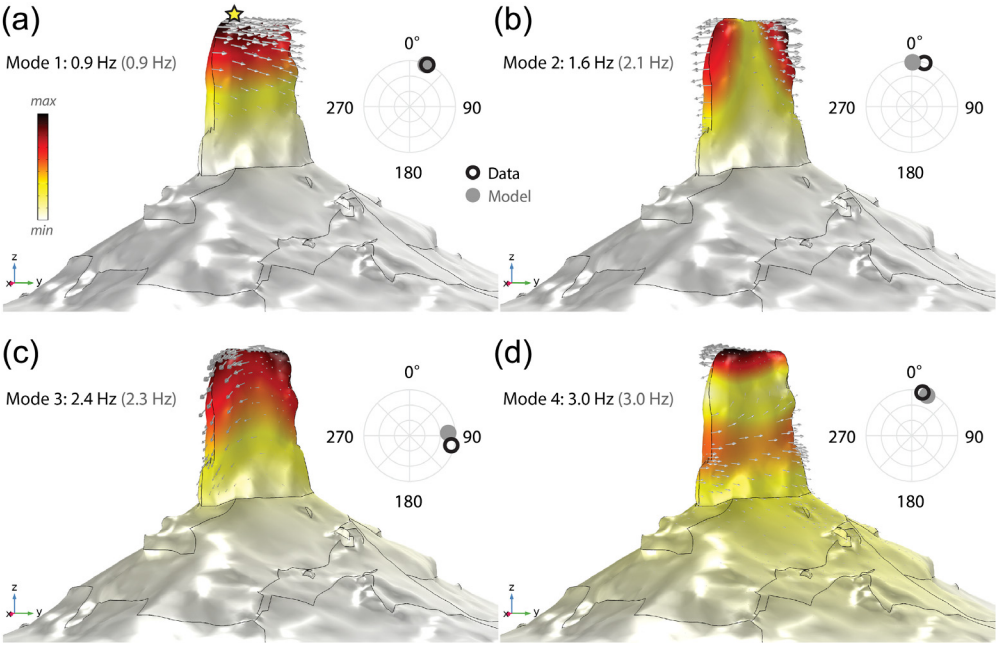

Figure 5. Numerical eigenfrequency results for Eagle Plume Tower (Fig. 1b; Table 1). (a) Mode 1, (b) mode 2, (c) mode 3, and (d) mode 4. Inset plots show stereographic projections of measured (black) and modeled (gray) natural frequencies and polarization vectors (in which 0 is the magnetic north and horizontal incidence angles plot on the circumference; vertical at center). Star in (a) is the location of the seismometer. Colors and arrows show scaled modal displacement relative to each mode. The color version of this figure is available only in the electronic edition.

allowed us to identify torsional modes (indicated in Fig. 4), which are not uniquely distinguished from bending modes in our field data using single-station polarization analysis. Figure 6 displays the fundamental mode of three towers of different scale (decreasing from 120 to 3 m high), showing these features share comparable mode shapes due to similar boundary conditions and overall geometry.

The analytical expression for an Euler–Bernoulli cantilever beam (equation 2) predicts that the fundamental frequency of rock towers, as well as fins, scales linearly with the ratio of a tower's width to its squared height (w/h^2). Our data spanning a range of feature scales show close agreement with this theoretical relationship (Fig. 7). In particular, we were able to use the lower-bound average Young's modulus and density for sandstone towers from our numerical models (E = 1 GPa, ρ = 2000 kg/m^3) to generate the theoretical line shown in Figure 7, which we suggest is representative of the softer sandstones studied here. Only the two very large sandstone towers deviate from this trend, each with higher fundamental frequency than anticipated, indicating higher Young's modulus values as also predicted for these features by our models (Table 1). Conglomerate towers also plot above sandstone features in our dataset (Fig. 7), suggesting these have higher Young's moduli.

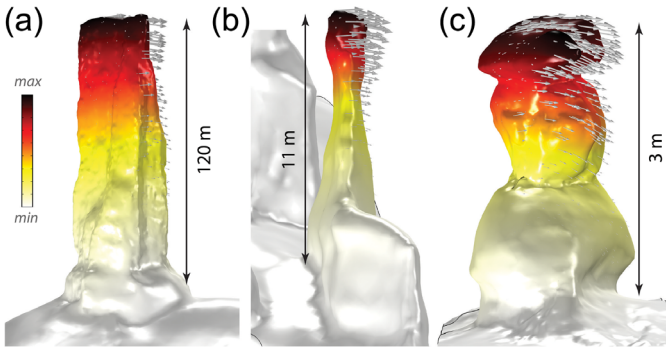

Figure 6. Simulated fundamental modes for three towers of different height (see inset scale bars): (a) Castleton Tower (f_0 = 0.8 Hz), (b) Skinny Witch (f_0 = 3.6 Hz), and (c) Bike Seat (f_0 = 10.5 Hz). Colors and arrows show scaled modal displacement relative for each mode. Each tower exhibits a displacement pattern resembling that of a simple cantilever. Modeled frequencies and polarization vectors match field data in each case indicating the simplified numerical models adequately reproduce measured tower behavior. The color version of this figure is available only in the electronic edition.

Data from 18 previously published sites are additionally compiled in Figure 7, indicating general agreement with the geometry–frequency trend described by equation (2). As predicted, stiffer limestone and carbonate materials plot above the softer sandstone towers, and the precipitated calcite cave stalagmites provide a possible upper limit estimate on the range of fundamental frequencies for stiff rocks (among the lithologies included). Overall, however, more scatter is apparent within the compiled data, as expected for sites with different lithologies, densities, and Young's moduli. Data generated in this study for the four features not successfully modeled also conform to the expected trend of fundamental frequency versus w/h^2 ratio (Fig. 7). Secret Spire (Fig. 1m) notably plots below the suggested lower-bound curve, as its asymmetric top-heavy profile deviates from the constant-thickness assumption of equation (2).

Discussion and Conclusions

We measured the resonance properties of 14 rock towers and fins of varying size, observing that the fundamental frequency

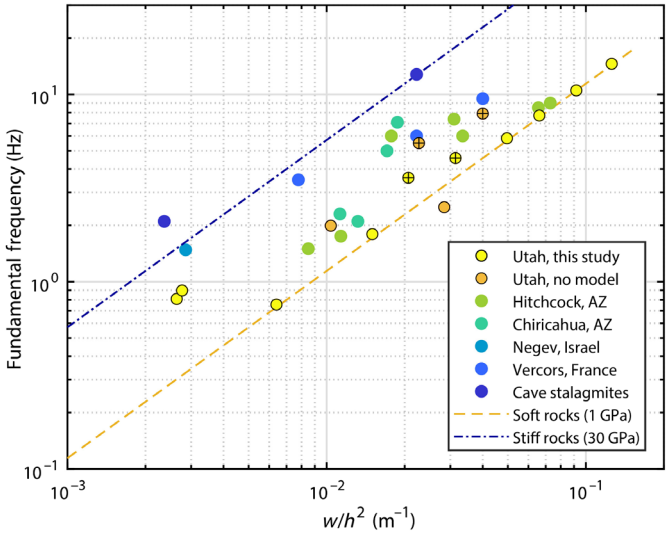

Figure 7. Fundamental frequency versus w/h^2 for all study sites, including previously published datasets (no marker outline; references in Study Sites section and Table S1). Conglomerate towers are marked with a cross. Equation (2) predicts a linear relationship with slope that is a function of material properties (in log–log space, the line shifts vertically). We bracket all data with two lines: the lower representing a possible end member for soft rocks drawing on our calibrated numerical models of sandstone features (here $\rho = 2000$ kg/m^3, $E = 1$ GPa), and the upper being a possible end member for stiff rocks (here $\rho = 2400$ kg/m^3, $E = 30$ GPa). The color version of this figure is available only in the electronic edition.

ranges between 0.8 and 15 Hz and generally scales with height (Table 1). The fundamental mode of all sites is full-height bending against the minor horizontal width (e.g., Fig. 6), identified via subhorizontal polarized motion measured on the top of the landform. Tower-like features (with nearly equal horizontal dimensions) generally exhibited another clear full-height bending mode as the second natural frequency, bending against the major horizontal axis, followed by torsion at mode three. Conversely, fin-like features generally exhibited torsion at mode two, with full-height bending against the major axis as mode three. Torsional modes may be more difficult to measure for narrow, tower-like features as it is more likely the sensor will be placed at or near the torsional node point along the tower's central axis, whereas for fins, the sensor can be placed on one end where larger torsional displacements are expected. Second-order bending modes were resolved in some of our datasets (e.g., Fig. 5), with predictable modal azimuths determined by landform orientation (both perpendicular and parallel to the major axis orientation). Our data further reveal relatively low-modal damping ratios (Fig. 3; Table 1), which we attribute primarily to low-radiation damping facilitated by limited cross-sectional basal areas. Similar damping ratios have been measured on rock arches (Geimer *et al.*, 2020; Häusler, Geimer, *et al.*, 2021), whereas features with larger basal or contact areas have correspondingly higher damping (e.g., Häusler, Michel, *et al.*, 2021). Damping (ζ) is theoretically linked to spectral amplification (A): for the fundamental mode of a continuous homogenous cantilever $A = 0.785/\zeta$ (Moore *et al.*, 2019). Therefore, our measured range of damping (0.6%–2.2%) suggests amplification factors of 35–130 are possible, with potentially important implications for seismic stability assessments.

We were able to reproduce field data using 3D numerical modal analysis for 10 of the 14 landforms assessed in this study (Fig. 4; Table S2). The successful matches between model and data indicate that the simplified assumption of uniform composition was satisfactory, and that given a relatively detailed geometrical model, the natural frequencies and mode shapes of rock towers can largely be predicted. Advantages of numerical modal analysis include a more detailed approximation of the modal deformation field, for example, highlighting areas of high strain, assessment of sensor placement for planning field measurements or evaluating undetected modes, and identification of torsional modes which are not uniquely distinguished from measurements using a single sensor. The models additionally generate estimates of Young's modulus for each landform when calibrated to match measured natural frequencies (Table 1). Young's modulus values determined in this study are consistent with previous modal analyses of rock arches in similar rock types (Geimer *et al.*, 2020), as well as limited available laboratory testing (Moore *et al.*, 2018), which indicate a typical range between ~1 and 10 GPa for sandstone. Higher values determined in this study likely reflect site-specific differences in material properties, such as calcite or iron content, and preferential occurrence at the largest two features indicates these differences may aid in landform survival. Aside from uniform composition, the selection of fixed boundary conditions represents a key assumption in these models. For features isolated from surrounding topography, selection of boundary conditions is straightforward (e.g., trimming the model to flat ground at the base); however, when the tower sits atop underlying topography, this may be less clear. In such models, like Eagle Plume Tower (Fig. 5), we experimented with progressively raising the lower model boundary until it reached the base of the tower, testing for differences in predicted modal properties between the full-scene and trimmed models. We found that the first three modes were unaffected by this trimming, however higher-order modes showed differences, especially in the full-scale models as they began to elastically incorporate underlying topography.

Moore *et al.* (2019) previously demonstrated that slender rock towers primarily deform in flexural bending (rather than shear), and suggested that modal deformation is similar to that of an idealized Euler–Bernoulli cantilever beam, a point also noted in other studies (e.g., Dowding *et al.*, 1983; Bottelin *et al.*, 2013; Finzi *et al.*, 2020; Martin *et al.*, 2020). Compilation of our data with similar previously published studies shows that fundamental frequencies of rock towers and fins scale to the first

order with a geometrical ratio as predicted for the analytical behavior of a cantilever (Fig. 7; equation 2). This indicates that the fundamental frequency of a rock tower can be estimated from measurements of geometry alone. The closeness of fit for most of our data to a linear trend arises in part because of the similar lithologies tested (most sites were sandstone), but also due to the shared regular geometries of the features. We note deviations for features with irregular geometry, such as Secret Spire. In these cases, the cantilever equation can be modified by a shape factor that accounts for differences from the assumed regular profile of a prismatic beam (see Dowding *et al.*, 1983). We bracket the data compilation in Figure 7 by two lines: one which we suggest as a lower limit for "soft" rocks ($\rho = 2000$ kg/m^3, $E = 1$ GPa), as constrained by our sandstone data, and another bracketing a plausible upper limit for stiff rocks indicated by previously published values (assuming $\rho = 2400$ kg/m^3, $E = 30$ GPa). These brackets add additional guidance in practical applications using the data compilation shown in Figure 7 to estimate fundamental frequencies of other rock towers and fins in different environments. However, the wide range of measured frequencies for a given w/h^2 ratio strongly limits the accuracy of such estimates.

Our results provide useful inputs for evaluating seismic stability and the potential for vibration damage of rock towers and fins. Certain vibration sources, for example, helicopters, emit narrowband energy (infrasound in this case; Finnegan *et al.*, 2021), whereas other anthropogenic sources such as blasts, trains, and other vehicle traffic generate ground-borne energy in a broader frequency range between ~1 and 20 Hz (Hunt, 1991; Lavoué *et al.*, 2021). Meanwhile, the spectral content of an earthquake measured at a given site varies depending on the magnitude, epicentral distance, and depth (e.g., Abrahamson *et al.*, 2014). In each case, evaluating structural damage or stability of rock towers from exposure to these sources benefits from estimates of resonance susceptibility using site-specific modal properties. During resonance, incoming energy is efficiently transferred to the oscillating system and metrics such as structural admittance (e.g., Finnegan *et al.*, 2021) or spectral acceleration (e.g., Finzi *et al.*, 2020) can be used to predict vibration amplitudes for various source parameters within a linear regime. These estimates may then be extended to determine conditions under which structural failure may occur, for example, by adopting the conceptual framework of a cantilever to calculate peak tensile stresses at or near the base of a tower. This approach may require additional refinement, however, to account for variations in landform response in high-strain nonlinear regimes, and in addition for most rock masses, transitioning from a continuum mechanics framework to fracture mechanics analyses (Eppes and Keanini, 2017). In each case, descriptions of landform natural frequencies, modal vectors, and damping ratios represent crucial data underpinning all subsequent vibration risk and seismic stability assessments.

Data and Resources

All data generated in this study are available for download at https://doi.org/10.7278/S50D-N12Q-SA1Z. The supplemental material contains figures describing spectral and polarization attributes of the towers in the study, details of the compiled dataset of towers, pillars, and pinnacles from this and previously published studies, comparison between measured and modeled modal attributes of 10 towers, and videos of simulated natural modes of vibration for Eagle Plume Tower, Utah. COMSOL Multiphysics software is available at www.comsol.com. Bentley's software is available at www.bentley.com. Meshmixer software is available at www.meshmixer.com. All websites were last accessed in September 2021.

Declaration of Competing Interests

The authors declare that there are no competing interests.

Acknowledgments

This study was funded by the National Science Foundation Grant EAR-1831283 and the University of Utah, Office of Undergraduate Research. The authors are grateful for field assistance from Clayton Russell, Avery Parrinello, Natan Richman, Weston Manygoats, Holly Hurtado, Henry Moore, Anne Moore, and Jerry Moore. Mauro Häusler and two anonymous reviewers provided valuable input for this article.

References

Abrahamson, N. A., W. J. Silva, and R. Kamai (2014). Summary of the ASK14 ground motion relation for active crustal regions, *Earthq. Spectra* **30,** no. 3, 1025–1055.

Ambrosini, R. D. (2006). Material damping vs. radiation damping in soil–structure interaction analysis, *Comput. Geotech.* **33,** no. 2, 86–92.

Baker, J. W., N. A. Abrahamson, J. W. Whitney, M. P. Board, and T. C. Hanks (2013). Use of fragile geologic structures as indicators of unexceeded ground motions and direct constraints on probabilistic seismic hazard analysis, *Bull. Seismol. Soc. Am.* **103,** 1898–1911.

Bottelin, P., L. Baillet, A. Carrier, E. Larose, D. Jongmans, O. Brenguier, and H. Cadet (2021). Toward workable and cost-efficient monitoring of unstable rock compartments with ambient noise, *Geosciences* **11,** no. 6, 242, doi: 10.3390/geosciences11060242.

Bottelin, P., L. Baillet, E. Larose, D. Jongmans, D. Hantz, O. Brenguier, H. Cadet, and A. Helmstetter (2017). Monitoring rock reinforcement works with ambient vibrations: La Bourne case study (Vercors, France), *Eng. Geol.* **226,** 136–145.

Bottelin, P., C. Lévy, L. Baillet, D. Jongmans, and P. Guéguen (2013). Modal and thermal analysis of Les Arches unstable rock column (Vercors massif, French Alps), *Geophys. J. Int.* **194,** no. 2, 849–858.

Branch, E., and D. Cordalis (2017). The unlawful reduction of bears ears national monument: An executive overreach, *Trends* **49,** 4.

Brune, J. N. (1996). Precariously balanced rocks and ground-motion maps for southern California, *Bull. Seismol. Soc. Am.* **86,** no. 1A, 43–54.

Carmean, K. (2002). *Spider Woman walks this Land: Traditional Cultural Properties and the Navajo Nation*, Vol. 8, Rowman, Altamira, Spain.

Çelebi, M. (2000). Radiation damping observed from seismic responses of buildings, *Proc. 12th World Conf. Earthquake Engineering*, Auckland, New Zealand, 20 January–4 February 2000.

Chopra, A. K. (2012). *Dynamics of Structures*, Pearson Education, Upper Saddle River, New Jersey, 944 pp.

Cole, H. A. (1973). On-line failure detection and damping measurement of aerospace structures by random decrement signatures,

Contract Rept. NASA-CR-2205, available at https://ntrs.nasa.gov/api/citations/19730010202/downloads/19730010202.pdf (last accessed January 2022).

Colombero, C., A. Godio, and D. Jongmans (2021). Ambient seismic noise and microseismicity monitoring of a prone-to-fall Quartzite Tower (Ormea, NW Italy), *Remote Sens.* **13,** no. 9, 1664, doi: 10.3390/rs13091664.

Dowding, C. H., F. S. Kendorski, and R. A. Cummings (1983). Response of rock pinnacles to blasting vibrations and airblasts, *Bull. Assoc. Eng. Geol.* **20,** no. 3, 271–281.

Eppes, M. C., and R. Keanini (2017). Mechanical weathering and rock erosion by climate-dependent subcritical cracking, *Rev. Geophys.* **55,** no. 2, 470–508.

Finnegan, R., J. R. Moore, and P. R. Geimer (2021). Vibration of natural rock arches and towers excited by helicopter-sourced infrasound, *Earth Surf. Dynam. Discuss.* doi: 10.5194/esurf-9-1459-2021.

Finzi, Y., N. Ganz, O. Dor, M. Davis, O. Volk, S. Langer, R. Arrowsmith, and M. Tsesarsky (2020). Stability analysis of fragile rock pillars and insights on fault activity in the Negev, Israel, *J. Geophys. Res.* **125,** no. 12, e2019JB019269, doi: 10.1029/2019JB019269.

Geimer, P. R., R. Finnegan, and J. R. Moore (2020). Sparse ambient resonance measurements reveal dynamic properties of freestanding rock arches, *Geophys. Res. Lett.* **47,** no. 9, e2020GL087239, doi: 10.1029/2020GL087239.

Gribovszki, K., S. Esterhazy, and G. Bokelmann (2018). Numerical modeling of stalagmite vibrations, *Pure Appl. Geophys.* **175,** no. 12, 4501–4514.

Häusler, M., C. Michel, J. Burjánek, and D. Fäh (2021). Monitoring the Preonzo rock slope instability using resonance mode analysis, *J. Geophys. Res.* doi: 10.1029/2020JF005709.

Häusler, M., P. R. Geimer, R. Finnegan, D. Fäh, and J. R. Moore (2021). An update on techniques to assess normal mode behavior of rock arches by ambient vibrations, *Earth Surf. Dynam.* **9,** no. 6, 1441–1457.

Hunt, H. E. M. (1991). Stochastic modelling of traffic-induced ground vibration, *J. Sound Vib.* **144,** no. 1, 53–70.

Incorporated Research Institutions for Seismology Data Management Center (IRIS-DMC) (2015). Data services products: Polarization attributes bundle, doi: 10.17611/DP/NTK.4.

King, K. (2001). Chiricahua Pinnacle Vibration Investigation, *National Park Service Contract Report*, 1–29.

King, K. (2003). Construction vibration studies for pinnacles and a natural bridge, *General Hitchcock Highway-Highway Project AZ PFD 39-1 (7)*, 1–19, available at https://citeseerx.ist.psu.edu/viewdoc/download?doi=10.1.1.563.1382&rep;=rep1&type;=pdf (last accessed January 2022).

Kleinbrod, U., J. Burjánek, and D. Fäh (2019). Ambient vibration classification of unstable rock slopes: A systematic approach, *Eng. Geol.* **249,** 198–217.

Koper, K. D., and R. Burlacu (2015). The fine structure of double-frequency microseisms recorded by seismometers in North America, *J. Geophys. Res* **120,** no. 3, 1677–1691.

Koper, K. D., and V. L. Hawley (2010). Frequency dependent polarization analysis of ambient seismic noise recorded at a broadband seismometer in the central United States, *Earthq. Sci.* **23,** no. 5, 439–447.

Lavoué, F., O. Coutant, P. Boué, L. Pinzon-Rincon, F. Brenguier, R. Brossier, P. Dales, M. Rezaeifar, and C. J. Bean (2021). Understanding seismic waves generated by train traffic via modeling: Implications for seismic imaging and monitoring, *Seismol. Res. Lett.* **92,** no. 1, 287–300.

Lévy, C., L. Baillet, D. Jongmans, P. Mourot, and D. Hantz (2010). Dynamic response of the Chamousset rock column (Western Alps, France), *J. Geophys. Res* **115,** no. F4, doi: 10.1029/2009JF001606.

Martin, A., T. Lecocq, K. G. Hinzen, T. Camelbeeck, Y. Quinif, and N. Fagel (2020). Characterizing stalagmites' Eigen frequencies by combining in situ vibration measurements and finite element modeling based on 3D scans, *Geosciences* **10,** no. 10, 418, doi: 10.3390/geosciences10100418.

McPhillips, D., and K. M. Scharer (2021). Survey of fragile geologic features and their quasi-static earthquake ground-motion constraints, Southern Oregon, *Bull. Seismol. Soc. Am.* doi: 10.1785/0120200378.

Michel, C., P. Guéguen, and P. Y. Bard (2008). Dynamic parameters of structures extracted from ambient vibration measurements: An aid for the seismic vulnerability assessment of existing buildings in moderate seismic hazard regions, *Soil Dynam. Earthq. Eng.* **28,** no. 8, 593–604.

Mikael, A., P. Gueguen, P. Y. Bard, P. Roux, and M. Langlais (2013). The analysis of long-term frequency and damping wandering in buildings using the random decrement technique, *Bull. Seismol. Soc. Am.* **103,** no. 1, 236–246.

Moore, J. R., P. R. Geimer, R. Finnegan, and C. Michel (2019). Dynamic analysis of a large freestanding rock tower (Castleton Tower, Utah, USA), *Bull. Seismol. Soc. Am.* **109,** no. 5, 2125–2131, doi: 10.1785/0120190118.

Moore, J. R., P. R. Geimer, R. Finnegan, and M. S. Thorne (2018). Use of seismic resonance measurements to determine the elastic modulus of freestanding rock masses, *Rock Mech. Rock Eng.* **51,** no. 12, 3937–3944.

Moore, J. R., M. S. Thorne, K. D. Koper, J. R. Wood, K. Goddard, R. Burlacu, S. Doyle, E. Stanfield, and B. White (2016). Anthropogenic sources stimulate resonance of a natural rock bridge, *Geophys. Res. Lett.* **43,** doi: 10.1002/2016GL070088.

Rood, A. H., D. H. Rood, M. W. Stirling, C. M. Madugo, N. A. Abrahamson, K. M. Wilcken, T. Gonzalez, A. Kottke, A. C. Whittaker, W. D. Page, *et al.* (2020). Earthquake hazard uncertainties improved using precariously balanced rocks, *AGU Adv.* **1,** e2020AV000182, doi: 10.1029/2020AV000182.

Silva, J. M. (1999). An overview of the fundamentals of modal analysis, in *Modal Analysis and Testing*, J. M. Silva and N. M. M. Maia (Editors), Kluwer Academic Publishers, Dordrecht, the Netherlands, 1–34.

Ward, K. M., and F. Lin (2017). On the viability of using autonomous three-component nodal geophones to calculate teleseismic Ps receiver functions with an application to old faithful, Yellowstone, *Seismol. Res. Lett.* **88,** 1268–1278, doi: 10.1785/0220170051.

Wu, S.-M., K. M. Ward, J. Farrell, F.-C. Lin, M. Karplus, and R. B. Smith (2017). Anatomy of Old Faithful from subsurface seismic imaging of the Yellowstone Upper Geyser Basin, *Geophys. Res. Lett.* **44,** 10,240–10,247, doi: 10.1002/2017GL075255.

Manuscript received 11 November 2021
Published online 16 February 2022